

Climate at high-obliquity

Article

Accepted Version

Ferreira, D., Marshall, J., O'Gorman, P. A. and Seager, S.
(2014) Climate at high-obliquity. *Icarus*, 243. pp. 236-248.
ISSN 0019-1035 doi:
<https://doi.org/10.1016/j.icarus.2014.09.015> Available at
<https://centaur.reading.ac.uk/37624/>

It is advisable to refer to the publisher's version if you intend to cite from the work. See [Guidance on citing](#).

To link to this article DOI: <http://dx.doi.org/10.1016/j.icarus.2014.09.015>

Publisher: Elsevier

All outputs in CentAUR are protected by Intellectual Property Rights law, including copyright law. Copyright and IPR is retained by the creators or other copyright holders. Terms and conditions for use of this material are defined in the [End User Agreement](#).

www.reading.ac.uk/centaur

CentAUR

Central Archive at the University of Reading

Reading's research outputs online

Climate at high-obliquity

David Ferreira^{a,*}, John Marshall^a, Paul A. O’Gorman^a, Sara Seager^a

^aDepartment of Earth, Atmospheric and Planetary Science, Massachusetts Institute of Technology, Cambridge, Massachusetts

Abstract

The question of climate at high obliquity is raised in the context of both exoplanet studies (e.g. habitability) and paleoclimates studies (evidence for low-latitude glaciation during the Neoproterozoic and the "Snowball Earth" hypothesis). States of high obliquity, ϕ , are distinctive in that, for $\phi \geq 54^\circ$, the poles receive more solar radiation in the annual mean than the Equator, opposite to the present day situation. In addition, the seasonal cycle of insolation is extreme, with the poles alternatively "facing" the sun and sheltering in the dark for months.

The novelty of our approach is to consider the role of a dynamical ocean in controlling the surface climate at high obliquity, which in turn requires understanding of the surface winds patterns when temperature gradients are reversed. To address these questions, a coupled ocean-atmosphere-sea ice GCM configured on an aquaplanet is employed. Except for the absence of topography and modified obliquity, the set-up is Earth-like. Two large obliquities ϕ , 54° and 90° , are compared to today’s Earth value, $\phi=23.5^\circ$.

*Corresponding author. Now at the Department of Meteorology, University of Reading, PO Box 243, Reading, RG6 6BB, UK.

Email address: d.g.ferreira@reading.ac.uk (David Ferreira)

Three key results emerge at high obliquity: 1) despite reversed temperature gradients, mid-latitudes surface winds are westerly and trade winds exist at the equator (as for $\phi=23.5^\circ$) although the westerlies are confined to the summer hemisphere, 2) a habitable planet is possible with mid-latitude temperatures in the range 300-280 K and 3) a stable climate state with an ice cap limited to the equatorial region is unlikely.

We clarify the dynamics behind these features (notably by an analysis of the potential vorticity structure and conditions for baroclinic instability of the atmosphere). Interestingly, we find that the absence of a stable partially glaciated state is critically linked to the absence of ocean heat transport during winter, a feature ultimately traced back to the high seasonality of baroclinic instability conditions in the atmosphere.

1. Introduction

Exoplanets, including those that have the potential to harbor life, are expected to have a range of obliquities. The reasoning is based both on the range of obliquities of the terrestrial planets of our own solar system as well as predictions for exoplanets. The obliquity of Mars has been shown to vary chaotically, ranging from zero to nearly sixty degrees (Laskar and Robutel, 1993; Touma and Wisdom, 1993). Venus has an obliquity close to 180 degrees, and therefore a retrograde rotation (Carpenter, 1964; Shapiro, 1967). While measurements of exoplanet obliquity are unlikely to be possible (but c.f. Carter and Winn (2010) for a specialized case), the final states of exoplanet obliquity evolution will be affected by gravitational tides and thermal atmospheric tides, core-mantle friction (Correia and Laskar, 2011;

13 Cunha et al., 2014), and collisions with other planets or planetesimals. A
14 large moon is also thought to play a stabilizing role on obliquity variations,
15 however it depends on the planet’s initial obliquity (Laskar et al., 1993). The
16 tidal evolution depends on a planet’s distance to its host star, which for hab-
17 itable zones changes for different star type. While a number of publications
18 have addressed the influence of obliquity on climates of Earth-like planets
19 none have considered a dynamic ocean (Gaidos and Williams, 2004; Spiegel
20 et al., 2009; Cowan et al., 2012; Armstrong et al., 2014).

21 If obliquity exceeds 54 degrees, polar latitudes receive more energy per
22 unit area, in the yearly mean, than do equatorial latitudes and undergo a
23 very pronounced seasonal cycle, a challenge for the development of life (Fig.
24 1 and further discussion below). A key aspect with regard to habitability is
25 to understand how the atmosphere and ocean of this high obliquity planet
26 work cooperatively together to transport energy meridionally, mediating the
27 warmth of the poles and the coldness of the equator. How extreme are
28 seasonal temperature fluctuations? Should one expect to find ice around the
29 equator?

30 Additional motivation for the study of climate at high obliquity is found
31 in Earth’s climate history which shows evidence of large low-latitude glacia-
32 tions during the Neoproterozoic (~ 700 -600 My ago). An interpretation is
33 that Earth was completely covered with ice at these periods, the so-called
34 ”Snowball Earth” hypothesis (Kirschvink, 1992; Hoffman et al., 1998). This
35 hypothesis raises challenging questions about the survival of life during the
36 long (~ 10 My) glacial spells and requires an escape mechanism out of a fully
37 glaciated Earth (see Pierrehumbert et al., 2011, for a review). An alternative

38 to the "Snowball Earth" state is that Earth was in a high obliquity configu-
39 ration with a cold equator and warm poles. The interpretation is then that
40 large ice caps existed in equatorial regions while the poles remained ice-free.
41 From a climate perspective (leaving aside other difficulties, see Hoffman and
42 Schrag, 2002), it is unclear if such a climate state can be achieved in the
43 coupled system. Recent work showed that the existence of large stable ice
44 caps critically depends on the meridional structure of the ocean heat trans-
45 port (OHT): sea ice caps extend to latitudes at which the OHT has maxima
46 of convergence (Rose and Marshall, 2009; Ferreira et al., 2011). To address
47 such questions, one needs to consider dynamical constraints on the ocean
48 circulation and understand the pattern of surface winds.

49 High values of obliquity particularly challenge our understanding of cli-
50 mate dynamics because the poles will become warmer than the equator and
51 we are led to consider a world in which the meridional temperature gradients,
52 and associated prevailing zonal wind, have the opposite sign to the present
53 earth, and the equatorial Hadley circulation exists where it is cold rather
54 than where it is warm.

55 The problem becomes even richer when one considers the dynamics of an
56 ocean, should one exist. The volume and surface area of a planet's ocean
57 is not known a priori and is expected to be highly variable from planet to
58 planet due to the stochastic nature of delivery of volatiles to a planet during
59 its early phase. While the surface area of an ocean contributes to a planet's
60 surface climate (see a series of arguments in Abe et al., 2011; Zsom et al.,
61 2013; Kasting et al., 2013; Seager, 2014) investigating ocean surface area
62 is beyond the scope of this paper. A deep Earth-like ocean, on the other

63 hand, allows for a system of 3-dimensional ocean currents that is able to
64 transport large amount of heat and mitigate harsh climates, like the Gulf
65 Stream and Meridional Overturning Circulation (MOC) do on our present-
66 day Earth (e.g. Seager et al., 2002; Ferreira et al., 2010). A central question
67 for the ocean circulation is then: what is the pattern of surface winds at
68 high obliquities?, for it is the winds that drive the ocean currents and MOC.
69 How do atmospheric weather systems growing in the easterly sheared middle
70 latitude jets and subject to a global angular momentum constraint, combine
71 to determine the surface wind pattern. Should one expect middle latitude
72 easterly winds? If not, why not?

73 Here, possible answers to some of these questions are sought by experi-
74 mentation with a coupled atmosphere, ocean and sea-ice General Circulation
75 Model (GCM) of an earth-like aquaplanet: i.e. a planet like our own but on
76 which there is only an ocean but no land. The coupled climate is studied
77 across a range of obliquities (23.5, 54 and 90 degrees).

78 The novelty of our approach is the use of a coupled GCM in which both
79 fluids are represented by 3d fully dynamical models. To our knowledge, previ-
80 ous studies of climate at high-obliquity only employed atmosphere-only GCM
81 or atmospheric GCM coupled to a slab ocean (e.g. Jenkins, 2000; Donnadieu
82 et al., 2002; Williams and Pollard, 2003). There, the ocean is treated as a
83 “swamp” without OHT or with a prescribed OHT or with a diffusive OHT.
84 Other studies are based on Energy Balance Models (EBM, see North et al.,
85 1981, for a review) in which dynamics is absent and all (atmosphere+ocean)
86 transports are represented through a diffusive process (e.g. Williams and
87 Kasting, 1997; Gaidos and Williams, 2004; Spiegel et al., 2009).

88 In our simulations, the OHT is realized as part of the solution. Our
89 approach allows us to document the ocean circulation at high-obliquity and
90 to explore, in a dynamically consistent way, the role of the ocean in setting
91 the climate. We present some of the descriptive climatology of our solutions
92 and how they shed light on the deeper questions of coupled climate dynamics
93 that motivate them. We focus on understanding the ocean circulation and its
94 forcing. This leads us into a detailed analysis of the mechanisms responsible
95 for the maintenance of surface winds. We notably elucidate the conditions for
96 baroclinic instability and storm track development in a world with reversed
97 temperature gradients. Our analysis of the atmospheric dynamics and energy
98 transports are also a novelty of this study.

99 We use an Aquaplanet set up, a planet entirely covered with a 3000 m-
100 deep ocean. The previous studies mentioned above used present-day and
101 Neoproterozoic continental distributions. One might be concerned by the
102 absence of topographical constraints in our Aquaplanet. Fig. 2 however illus-
103 trates that the energy transports simulated in Aquaplanet at $\phi=23^\circ$ compare
104 favorably with present-day observed transports (in terms of shape, magni-
105 tude and partitioning between ocean and atmosphere – see further discussion
106 in Marshall et al. (2007)). That is, the main features of the ocean and atmo-
107 sphere circulations of our present climate are well captured in an Aquaplanet
108 set-up. Although continental configurations can influence the climate state
109 and are indeed important to explain some aspects of present and past Earth’s
110 climate (Enderton and Marshall, 2009; Ferreira et al., 2010), such a level of
111 refinement is not warranted for a first investigation of the coupled system at
112 high obliquity.

113 A short description of our coupled GCM is given in section 2. Section 3
 114 focuses on the atmospheric dynamics and the maintenance of surface wind
 115 patterns. Energy transports and storage in the coupled system are described
 116 in section 4. Implication of our results for exoplanets’ habitability and Snow-
 117 ball Earth are discussed in section 5. Conclusions are given in section 5. An
 118 appendix briefly describes simulations at 54 obliquity.

119 **2. The coupled GCM**

120 We employ the MITgcm (Marshall et al., 1997) in a coupled ocean-
 121 atmosphere-sea ice “aquaplanet” configuration. The model exploits an iso-
 122 morphism between the ocean and atmosphere dynamics to generate an atmo-
 123 spheric GCM and an oceanic GCM from the same dynamic core (Marshall
 124 et al., 2004). Along with salinity (ocean) and specific humidity (atmosphere),
 125 the GCMs solve for potential temperature, the temperature that a fluid parcel
 126 would have if adiabatically returned to a reference surface pressure (tradition-
 127 ally expressed in Celsius in the ocean and in kelvin in the atmosphere). All
 128 components use the same cubed-sphere grid at coarse C24 resolution (3.75°
 129 at the equator), ensuring as much fidelity in model dynamics at the poles as
 130 elsewhere. The ocean component is a primitive equation non-eddy-resolving
 131 model, using the rescaled height coordinate z^* (Adcroft et al., 2004) with 15
 132 levels and a flat bottom at 3 km depth (chosen to approximate present-day
 133 ocean volume, and thus total heat capacity). Convection is implemented
 134 as an enhanced vertical mixing of temperature and salinity (Klinger et al.,
 135 1996). Vertical background diffusivity is uniform at $3 \times 10^{-5} \text{ m}^2 \text{ s}^{-1}$. Ef-
 136 fects of mesoscale eddies are parametrized as an advective process (Gent and

137 McWilliams, 1990, hereafter GM) and an isopycnal diffusion (Redi, 1982).
 138 In the Redi scheme, temperature and salinity are diffused along surfaces of
 139 constant density, not horizontally. The GM scheme is a parametrization
 140 based on first principles: 1) it flattens isopycnal surfaces releasing available
 141 potential energy, hence mimicking baroclinic instability and 2) it is adiabatic
 142 (i.e conserves water masses properties). In contrast to the (unphysical and
 143 deprecated) horizontal mixing scheme, these two eddy schemes capture the
 144 quasi-adiabatic nature of eddy mixing in the ocean interior and simulate an
 145 oceanic flow regime similar to that observed in our oceans. The Redi and GM
 146 eddy coefficients are both set to $1200 \text{ m}^2 \text{ s}^{-1}$. As for the vertical diffusivity,
 147 these values are typically observed in Earth’s oceans.

148 The atmosphere is a 5-level¹ primitive equation model with moist physics
 149 based on SPEEDY (Molteni, 2003). These include a four-band long and
 150 shortwave radiation scheme with interactive water vapor channels, diagnostic
 151 clouds, a boundary layer parameterization and mass-flux scheme for moist
 152 convection. Details of these parameterizations (substantially simpler than
 153 used in high-end models) are given in Rose and Ferreira (2013). Present-
 154 day atmospheric CO_2 is prescribed. Insolation varies seasonally but there
 155 is no diurnal cycle (eccentricity is set to zero and the solar constant S_0
 156 to 1366 W m^{-2}). Despite its simplicity and coarse resolution, the atmo-
 157 spheric component represents the main features of Earth’s atmosphere, in-
 158 cluding vigorous midlatitudes synoptic eddies, an Intertropical Convergence
 159 Zone and Hadley Circulation, realistic precipitation patterns, and top-of-the-

¹Tick marks on the pressure axis of Figs. 3 and 8 correspond to the mid- and interface
 levels of the vertical grid, respectively.

160 atmosphere longwave and shortwave fluxes (see Molteni, 2003, for a detailed
161 description).

162 The sea ice component is a 3-layer thermodynamic model based on Win-
163 ton (2000) (two layers of ice plus surface snow cover). Prognostic variables
164 include ice fraction, snow and ice thickness, and ice enthalpy accounting
165 for brine pockets with an energy-conserving formulation. Ice surface albedo
166 depends on temperature, snow depth and age (Ferreira et al., 2011). The
167 model achieves machine-level conservation of heat, water and salt, enabling
168 long integrations without numerical drift (Campin et al., 2008). The reader
169 is referred to Ferreira et al. (2010) for further details about the set-up.

170 Integrations of the coupled system (to statistical equilibrium) are carried
171 out for three values of obliquity ϕ : 23.5, 54, and 90 degrees (Aqua23, Aqua54,
172 and Aqua90, respectively). All other parameters remain the same. We em-
173 phasize here that our focus is on an Earth-like coupled system, including a
174 consistent set of parameterizations and parameter values. We do not expect
175 our main conclusions to be very sensitive to these choices if varied within the
176 range of observationally constrained values. However, it is conceivable that
177 ocean and atmosphere on exoplanets sit in very different regimes than those
178 of Earth. For example, on present-day Earth, half of the energy required
179 for vertical mixing is provided by the dissipation of tides on the ocean floor:
180 ocean mixing could be very different on a moon-less planet. Exploration of
181 such a scenario is beyond the scope of this paper.

182 **3. Momentum transport: maintenance of the surface winds**

183 *3.1. Insolation and Temperature distribution*

184 For present-day obliquity ($\phi=23.5^\circ$), the annual-mean incoming solar ra-
185 diation at the top of the atmosphere is largest at the Equator and decreases
186 by $\sim 50\%$ toward the poles (Fig. 1, top). At $\phi=90^\circ$, the pattern is reversed,
187 with a Pole-to-Equator decrease of about 30%. For $\phi=54^\circ$, the profile is
188 nearly flat.

189 Over the seasonal cycle, all three obliquities show rather similar behaviors.
190 The summer/winter hemisphere contrast, however, is the strongest at $\phi=90^\circ$
191 and the weakest at $\phi=23.45^\circ$ (and would disappear for $\phi=0^\circ$). It is the
192 amplitude of the seasonal contrast that dictates the annual mean values.
193 At $\phi=23.5^\circ$, the equator receives a steady $\sim 400 \text{ W m}^2$ throughout the year
194 while the solar input at the poles barely reaches 500 W m^2 in summer and
195 vanishes in winter. During Boreal winter at $\phi=90^\circ$, the Northern Hemisphere
196 (NH) is almost completely in the dark while the South pole receives a full
197 1300 W m^2 . In contrast, the Equator oscillates between a medium solar input
198 ($\leq 500 \text{ W m}^2$) and near darkness, and so has a modest annual-mean value.

199 Focusing on the 90° case, the annual-mean potential temperature distri-
200 bution reflects the annual mean insolation (Fig. 3, top left): cold at the
201 equator and warm at the poles. Interestingly, we observe a rather mild cli-
202 mate, with surface temperatures within a narrow range (275-295 K) and
203 a weak Equator-to-Pole differences of 20 K. For comparison, Equator-to-
204 Pole differences are about 30 K in Aqua23 and in the present-day climate.
205 These annual-mean Equator-to-Pole temperature differences largely reflect
206 the annual-mean Equator-to-Pole insolation contrast.

207 The climate exhibits more surprising features on a seasonal basis. In
 208 January (Fig. 4, top left), despite the long NH darkness, the north pole
 209 remains well above freezing point (the minimum temperature of 285 K is
 210 reached in March) while temperatures at the South pole, receiving about
 211 1300 W m^2 , “only” reach 315 K. For comparison, in a simple EBM without
 212 meridional heat transport and a small heat capacity (no ocean), Armstrong
 213 et al. (2014) find that polar temperatures at $\phi=90^\circ$ vary from 217 K to 389 K,
 214 a 170 K seasonal amplitude, compared to 30 K here.

215 In the ocean Fig. 4, we also observe a cold Equator and warm poles and
 216 in reverse to present day conditions, a large stratification is found at the pole
 217 and a weak stratification at the Equator. Seasonal variations are restricted
 218 to the upper 200 m. In January, the upper ocean warms up to 26°C at the
 219 South Pole and cools down to 14°C at the North pole. The Equator remains
 220 at a steady 2°C (again well above the freezing point, about -1.9°C for our
 221 salty ocean).

222 How are such mild annual mean temperatures and weak seasonal varia-
 223 tions achieved at $\phi=90^\circ$, despite the large incoming solar fluctuations? One
 224 can isolate three main mechanisms that ameliorate the extremes: atmo-
 225 spheric energy transport, oceanic energy transport and seasonal heat storage
 226 in the ocean. Fig. 5 shows the ocean, atmosphere and total energy trans-
 227 ports. The annual transports are equatorward nearly everywhere (in opposite
 228 direction to the transports seen at 23.5° obliquity and on Earth, see Fig. 2),
 229 but directed down the large-scale temperature gradient. Interestingly, both
 230 ocean and atmosphere transports are essentially limited to one season. They
 231 are large during summertime and nearly vanish in winter (see for example

232 January in Fig. 5).

233 Both ocean and atmosphere energy transports are a consequence of at-
234 mospheric circulation, directly in the atmosphere and indirectly in the ocean,
235 which is of course driven by surface winds. In this context, a key question is
236 to understand the development of synoptic scale eddies in the atmosphere.
237 Synoptic systems facilitate these transports: in the atmosphere, they are
238 very efficient at transporting energy while their eddy momentum fluxes also
239 maintain the surface winds which drive the ocean:

$$\overline{\tau_x} = - \int_0^\infty \partial_y (\overline{\rho u' v'}) dz \quad (1)$$

240 where τ_x is the zonal surface wind stress applied to the ocean, ρ the density
241 of air, overbars denote a time and zonal average, and primes a deviation from
242 this average.

243 We now go on to explore the dynamics of the atmospheric circulation of
244 Aqua90.

245 *3.2. Development of the storm track*

246 Since the circulation in Aqua90 is very strongly seasonal, we will focus
247 on one month of the year, January, which corresponds to wintertime in the
248 NH and summertime in the SH. In January, large temperature gradients
249 (~ 40 K) develop in the mid-latitudes of the SH (Fig. 4, top right). In the
250 NH, temperature gradients are very weak (~ 10 K), partly because there is
251 little contrast of incoming solar radiation across the hemisphere (Fig. 1,
252 bottom) and partly because the atmosphere is nearly uniformly heated from
253 below by the ocean (see below).

254 To determine the propensity to baroclinic instability, we compute the
 255 meridional gradients of mean quasigeostrophic potential vorticity (QGPV)
 256 \bar{q}_y :

$$\bar{q}_y = \beta - \bar{u}_{yy} + f^2 \frac{\partial}{\partial p} \left(\frac{1}{\tilde{R}} \frac{\bar{u}_p}{\bar{\theta}_p} \right) \quad (2)$$

257 where \bar{u} is the mean zonal wind, $\bar{\theta}$ the mean potential temperature, f the
 258 Coriolis parameter and β its meridional gradient, and \tilde{R} is the gas constant
 259 times $(p/p_o)^\kappa p^{-1}$ (with $\kappa=2/7$ and $p_o=1000$ mb the reference surface pres-
 260 sure).

261 The QGPV gradient is computed on model levels and the discretization
 262 of Eq. (2) accounts for the upper and lower boundary conditions, following
 263 the approach of Smith (2007). That is, the QGPV gradient shown in Fig.
 264 6 effectively includes a representation of the top and bottom PV sheets,
 265 as in the generalized PV definition of Bretherton (1966). In the pressure
 266 coordinate system used here, we approximate $\omega=0$ at the surface (the vertical
 267 velocity ω is exactly zero at the top of the atmosphere). The relative vorticity
 268 term \bar{u}_{yy} is neglected in Fig. 6 (it is only significant on scales smaller than
 269 the Rossby radius of deformation L_R , typically $L_R \simeq 800 - 1000$ km): its
 270 inclusion does not change our conclusion but results in noisier plots.

271 In Aqua23, \bar{q}_y is negative near the surface and positive throughout the
 272 troposphere: the surface temperature gradient dominates over β near the
 273 surface while the stretching term (due to sheared wind) reinforce β aloft
 274 (see Fig. 7, top, for the zonal wind profiles). Both hemispheres exhibit
 275 a clear gradient reversal in the vertical (slightly larger in the SH) and the
 276 (necessary) condition for baroclinic instability is satisfied (Charney-Stern
 277 criteria). Storm tracks are thus expected to develop in both hemispheres.

278 In Aqua90, however, surface temperature gradients are reversed and now
 279 reinforce the β contribution. Hence, surface QGPV gradients \bar{q}_y in Aqua90
 280 are positive and large, particularly in the summer hemisphere. In the mid-
 281 troposphere, the strongly easterly sheared winds in the Summer hemisphere
 282 result in a negative stretching term, large enough to overcome β . There
 283 is a clear (and ample) gradient reversal in the SH. In contrast, in the NH,
 284 where temperature gradients and wind shear are weak, \bar{q}_y is one-signed and
 285 dominated by β (except close to the surface where both β and the surface
 286 temperature contribution combine). We thus expect a storm track to develop
 287 in the SH, but not in the NH.

288 This is indeed the case as shown by the Reynolds stresses $\overline{u'v'}$ developing
 289 near 30-40°S in January (Fig. 7, top left) and the large eddy heat flux in
 290 the atmosphere at these latitudes (Fig. 9, bottom). The presence of a storm
 291 track is also revealed by large-scale precipitation in the mid-latitudes (due
 292 to the equatorward advection in synoptic eddies of warm-moist air parcels
 293 toward the cold Equator, see Fig. 8, bottom).

294 The negative Reynolds stresses in the SH can be interpreted as due to
 295 Rossby waves propagating away from the baroclinically unstable zone into
 296 the Tropics (see Held, 2000). Consistent with Eq. (1), the eddy momentum
 297 convergence sustains surface westerly winds near 50°S and trades winds in
 298 the deep tropics (Fig. 7).

299 It is interesting to contrast Aqua90's stability properties with those of
 300 Aqua23. Consistent with the QGPV analysis above, storm-tracks are co-
 301 existing in summer and winter hemispheres, as evidenced by the large (pole-
 302 ward) eddy momentum fluxes in both hemispheres (Fig. 7 top right). As a

consequence, surface westerly winds are sustained in the midlatitudes at all seasons, as well as a sizable eddy energy transport (not shown). The persistence of surface winds is key for understanding the oceanic temperature structure (see below). In Aqua90, surface winds vanish in winter because there are no eddies to sustain them.

In Aqua90, the atmospheric meridional overturning circulation in January (Fig. 8, top) is thermally direct as in Aqua23 (upwelling in the summer/southern hemisphere and downwelling in the winter/northern hemisphere)², but has an hemispheric latitudinal extent. This circulation is likely the result of the merging of the Ferrel and Hadley cells. The Ferrel cell is expected to be clockwise given the sense of the eddy momentum fluxes in the upper troposphere (Fig. 7, upper left). Meanwhile, the Hadley cell in the SH is expected to be reversed (compared to the low obliquity case) because of the reversed temperature gradient. As a result, the two cells circulate in the same sense and appear as one single cell. In July, the upwelling branch approaches the North pole and the overturning cell is of counterclockwise from 5°S to 70°N (not shown).

4. Energy transports and storage

4.1. The ocean and atmosphere energy transports

In Aqua90, the ocean and atmosphere both transport energy northward in January, i.e. from the summer to the winter hemisphere and down the

²The jump of the Hadley circulation out of the boundary layer between 5°S and 0° may be explained by the mechanism of Pauluis (2004).

324 large-scale temperature gradient. This is readily rationalized following the
325 previous analysis in section 3.

326 The decomposition of the AHT into mean and eddy components is shown
327 in Fig. 9. In January (bottom), both components are northward nearly ev-
328 erywhere, from the warm into the cold hemisphere. The large eddy heat flux
329 in the SH and near zero flux in the NH are consistent with the development
330 of baroclinic instability in the summer hemisphere only. The down-gradient
331 direction of the flux is associated with the extraction of available potential
332 energy from the mean flow. The eddy heat flux peaks near 50°S at 5 PW, a
333 value comparable to that seen in Aqua23 (although in the latter case eddy
334 heat fluxes exist in both hemispheres).

335 The transport due to the mean flow (largely the axisymmetric Hadley
336 circulation as there is no stationary wave component in our calculations)
337 accounts for most of the atmospheric heat transport in the tropics and all of
338 it in the Northern Hemisphere. Even at the latitudes of the storm track the
339 mean component is not negligible. This is in contrast with Aqua23 where
340 the mean flow contribution to AHT is small everywhere except in the deep
341 tropics.

342 Note that the AHT associated with the Hadley circulation has a strong
343 symmetry around the Equator. Therefore, the July (not shown) and January
344 Hadley cell transports largely oppose one another. In the annual mean, the
345 mean circulation contribution nearly cancels out and the AHT is dominated
346 by the eddy flux transport (Fig. 9, top).

347 The January OHT also transports heat from the pole toward the Equator
348 (Fig. 5). It is dominated by the contribution from mean Eulerian currents

349 (not shown). The Eulerian overturning (Fig. 7, bottom left) consist of a
 350 series of Ekman wind-driven cells matching the surface wind pattern (mid-
 351 dle). The OHT achieved by such circulation is well captured by the scaling
 352 $OHT \sim \Psi \sim \rho_o C_p \Delta T$ where Ψ is the strength of the circulation (in Sv), and
 353 ΔT is the vertical gradient of temperature (see Czaja and Marshall, 2006).
 354 The clockwise circulation between 0° and 25°N is very intense, reaching up
 355 to 400 Sv. However, because it acts on a very weak vertical temperature
 356 difference $\Delta T \sim 0$ (see Fig. 4 right), its contribution to the OHT is small
 357 (similarly for the cell between 5°S and 0° .) The SH midlatitude MOC cell
 358 is relatively weak (~ 15 Sv), but acts on a strong vertical gradient (notably
 359 sustained by the intense surface solar radiation). As the surface warm wa-
 360 ters are pushed equatorward by the winds and replaced by upwelling of cold
 361 equatorial deep water, the OHT achieved by the mid-latitude wind driven
 362 cell is equatorward, close to 4 PW (Fig. 5).

363 It is interesting to note that the (parameterized) eddy-induced transports
 364 in the ocean are negligible outside the deep tropics (not shown). This is not
 365 the case in Aqua23 where eddy processes are order one in the momentum
 366 and heat balance of the ocean (see Marshall et al., 2007). The absence of
 367 a significant eddy transport in Aqua90 is a consequence of the small slope
 368 of isopycnal surfaces³ (except close to the Equator, see Figs. 3 and 4). In
 369 comparison, steeply tilted isopycnals extend to a depth of 1000 m or more in

³To contrast with the previous discussion of PV gradients in the atmosphere, note that the eddy parameterization of Gent and McWilliams (1990) used here is not based on PV mixing (although it approximates it under some assumptions). Rather, it pre-supposes and represents release of available potential energy stored in tilting isopycnal surfaces.

370 Aqua23 (Fig. 3, bottom). The thermocline structure reflects the near perma-
371 nent pattern of surface winds (polar easterlies, midlatitudes westerlies, trade
372 winds) and associated Ekman pumping/suction. In Aqua90, surface winds
373 come and go seasonally, disallowing the building of a permanent thermocline.
374 Instead isopycnal surfaces remain relatively flat.

375 In Aqua90 as in Aqua23, the AHT has a broad hemispheric shape, peak-
376 ing in the mid-latitudes (compare Fig. 2 to Fig. 5). In Aqua23 (as in
377 observations), the OHT is large in the subtropics decreasing poleward, with
378 large convergences in the midlatitudes. It has a distinctly different shape
379 from that of the AHT. In Aqua90 however, the OHT is a “scaled down (by
380 a factor 2) version” of AHT (on the seasonal and annual timescales) and has
381 an hemispheric extent. In January, the OHT in Aqua90 converges at the
382 Equator and vanishes in the Northern/winter hemisphere.

383 *4.2. Ocean heat storage*

384 The upper ocean also contributes in modulating seasonal extremes of tem-
385 perature through seasonal storage of heat. In summer the ocean stores large
386 amounts of heat, mostly by absorbing shortwave radiation, and thus delaying
387 the increase of surface temperatures through the summer. As a consequence,
388 the summer hemisphere upper ocean is strongly stratified (Fig. 4).

389 In winter, heat stored in summer is released to the atmosphere. Large
390 amounts of heat are accessed through ocean convection which occupies the
391 entire northern hemisphere in January and much of it in March (note also the
392 deepening of the convective mixing as winter progresses, Fig. 4). The heat-
393 ing of the atmosphere from below is reflected in the fact that precipitation
394 is largely of convective origin in the winter hemisphere (an effect probably

395 amplified by the lack of stabilizing atmospheric eddies, Fig. 8, bottom).
 396 As a result, the atmosphere is effectively heated from below during winter.
 397 The solar heating is very weak (less than 10 W m^{-2} north of 25°N , see Fig.
 398 10) while the top-of-the-atmosphere longwave cooling is nearly uniform at
 399 about 240 W m^{-2} . This cooling is almost exactly balanced by air-sea fluxes
 400 ($\sim 220 \text{ W m}^{-2}$, mostly due, in equal fraction, to latent heat release and long-
 401 wave emission from the ocean surface, see Fig. 10, left).

402 The ocean plays a role in ameliorating temperature swings in two ways:
 403 1) it supplements the AHT by transporting energy from the summer to the
 404 winter hemisphere and 2) it stores heat in summer and releases it to the
 405 atmosphere in winter. What is the relative contribution of these two effects?

406 To compare them, we compute the OHT implied by the net air-sea heat
 407 fluxes, i.e. the meridional (and zonal) integral of the air-sea heat fluxes
 408 (starting from the North pole here). The difference between the actual and
 409 implied OHTs would be zero if there was no ocean heat storage (and indeed,
 410 on annual average, the two quantities are identical – not shown). In January
 411 (Fig. 10, right), the implied OHT reaches 50 PW at 20°S , that is 50 PW of
 412 heat are transferred from the atmosphere into the ocean south of 20°S and
 413 from the ocean into the atmosphere north of it. Clearly, only a small fraction
 414 (4 PW , less than 10%)⁴ of the air-sea flux is transported meridionally by the
 415 OHT, the remaining 90% being stored locally to be released the following
 416 season. In fact, even the AHT appears to play a secondary role on seasonal
 417 timescales. Within each hemisphere, the coupled ocean-atmosphere system

⁴In Aqua23, this fraction is substantially larger, about 30% (an OHT of 7 PW for an implied OHT of 20 PW) although the ocean heat storage remains the dominant effect.

behaves as a 1d column, storing and releasing heat over the seasonal cycle.

5. Implications

5.1. Habitability: the role of the ocean

The surface climates of 90 and 54° obliquity planets are mild, in fact milder than in Aqua23, a surprising result in perspective of the extreme summer insolation/long polar nights at high obliquity. These conclusions are similar to those of previous studies employing atmospheric GCMs coupled to 'swamp' ocean models, i.e. a motionless ocean without OHT (Jenkins, 2000; Williams and Pollard, 2003). This is expected from our analysis in section 4: the storage capability of the ocean largely overwhelms its dynamical contribution, the OHT.

To confirm this, we couple the atmospheric component of our coupled GCM to a "swamp" ocean. Three experiments at 90 degree obliquity are carried out with mixed layer depths of 10, 50 and 200 m, all initialized with uniform SST at 15°C. Here we explore the extreme short timescale temperature fluctuations.

Statistics of the Surface Air Temperature (SAT) over the Southern Hemisphere polar cap (90-55°S) are shown in Fig. 11 for the slab-ocean and coupled experiments. For each month of the year, the monthly-mean SAT averaged over the polar cap (90-55°S) is plotted along with typical extreme values. The latter are the averages (over 20 years) of the minimum and maximum values reached within a given month over the polar cap. This gives a sense of the temperature fluctuations generated by weather systems for each month of the year.

442 As seen previously, seasonal temperature changes in the coupled system
443 are mild. We also observed that temperature fluctuations within a given
444 month are also relatively small: the largest fluctuations are found in summer
445 with day-to-day changes of 20°C (in January). Slab-ocean simulations with
446 50 and 200 m mixed-layer depth exhibit SAT statistics similar to those seen
447 in the coupled GCM. The case of a 10 m deep slab ocean is remarkable as it
448 shows a collapse in a near Snowball state. This is obviously a catastrophic
449 outcome for habitability (see further discussion below).

450 The 50 and 200 m deep cases noticeably differs from the coupled system on
451 two aspects. First, minimum wintertime temperature are higher with a slab
452 ocean. This is probably because a slab ocean is more efficient at storing heat
453 in the summer because it has no compensating OHT toward the Equator. As
454 a result, slab-ocean runs exhibit even weaker seasonal fluctuations than the
455 coupled system. Second, the magnitude of day-to-day fluctuations increase
456 with slab oceans (35°C at 50 m depth). This is to be expected as temperature
457 changes in a dynamical ocean are damped by advection by the mean currents,
458 fluctuations in Ekman currents, upper ocean convection etc.

459 Although effects of a dynamical ocean are noticeable on SAT statistics,
460 the slab-ocean simulations closely reproduce the surface climate of the cou-
461 pled simulation, provided that the ocean is deep enough to avoid a Snowball
462 collapse. In an exoplanet context, in which the volume of ocean could be con-
463 sidered as a free parameter, our simulations suggest that the range of oceanic
464 depths that are critical to climate is rather small, say 0 to 100 m (i.e. a water
465 column with a heat capacity up to 100 times that of an atmospheric column
466 for our Earth-like set up). Depth variations beyond these values would only

467 result in small adjustments to the habitability.

468 5.2. *Collapse into a completely ice-covered state*

469 We showed in previous works that the coupled Aquaplanet at 23.5 degree
470 of obliquity can support a cold state with large ice caps extending from the
471 poles into the mid-latitudes and ice-free equatorial regions (Ferreira et al.,
472 2011). An analogous state at high-obliquity would present an ice cap around
473 the Equator extending poleward into the mid-latitudes and ice free poles.
474 Such a state of limited glaciation would avoid the challenges of a complete
475 "Snowball Earth" (e.g. the survival of life, an escape mechanism). Is such a
476 state possible?

477 To search for this solution, we carry out an experiment in which the
478 solar constant is lowered by small increments starting from the Aqua90 state
479 described previously. Lowering of the solar constant results in small cooling
480 until a dramatic global cooling for $S_o/4=338 \text{ W m}^{-2}$. At the transition, the
481 sea ice cover jumps, within a century, from 2% of the global area to 90% and
482 stabilizes around this value (Fig. 12). In the latter state, ice is present at all
483 latitudes: the globally averaged 90% ice coverage is only due to somewhat
484 reduced ($\sim 75\%$) ice concentrations around the poles. In other words, we do
485 not observe an intermediate state with a partial glaciation.

486 Interestingly, the same behavior is observed in the slab-ocean model.
487 While the solutions with 200 and 50 m deep mixed-layer converges to tem-
488 perate ice-free solution, the 10 m deep slab-ocean simulation collapsed into
489 a near-complete Snowball state (Fig. 11). Note that, a 50 m mixed-layer
490 simulation initialized with uniformly cold temperatures (5°C) similarly col-
491 lapses in a Snowball state. As in the fully ice-covered state of the coupled

492 model, above freezing temperatures and partial sea ice coverage ($\sim 75\%$) are
 493 found at the poles in the summer because of the intense shortwave radiation.
 494 These results are consistent with simulations by Jenkins (2000) and
 495 Donnadieu et al. (2002) with atmospheric GCMs coupled to slab oceans.
 496 For various choices of atmospheric CO_2 , solar constant and high obliquity,
 497 Jenkins (2000) observed mild climates or Snowball collapse. In Donnadieu
 498 et al. (2002), simulations with realistic configurations initialized from ice-free
 499 states rapidly converged to a nearly global glaciation⁵.

500 In the context of existence of multiple climate equilibria, we showed that
 501 a large ice cap solution in Aqua23 is possible because of the meridional structure
 502 of the OHT which peaks around 20°N/S to decrease sharply poleward
 503 (see Fig. 2). The associated OHT convergence can stop the expansion of sea
 504 ice into the mid-latitude, notably in winter (not shown), thus avoiding the
 505 collapse into a Snowball state (see also Poulsen and Jacob, 2004; Rose and
 506 Marshall, 2009). It is therefore not surprising that slab ocean configurations
 507 without OHT would exhibit either ice-free states or near global glaciations.
 508 As soon as sea ice appears even in very small amount (2% of the global cover
 509 here), there is no mechanism to stop the sea-ice albedo feedback. This also

⁵In both studies as in our slab and coupled simulations, summer ice concentration near the poles is below 100%. Note however that, in our simulations the sea ice thickness (which is not artificially limited) continues to increase rapidly, even as the sea ice area is equilibrated, to reach tens of meter within 200 years. Simulations of a steady state would require taking geothermal heating into account. This is beyond the scope of this paper: it is likely however that ice would grow hundreds of meter thick (for typical geothermal flux) and that ice flows would eventually enclose the globe into a hard Snowball state.

510 explains why shallow slab oceans are more susceptible to global glaciations:
511 their small thermal inertia makes it comparatively easier to approach the
512 freezing point within a winter season and initiate the ice-albedo feedback.

513 But, why does the dynamical ocean behave like a swamp? This answer
514 can be traced back to the seasonality of the storm track activity and surface
515 wind field. As discussed in sections 3 & 4, there are virtually no wind stress
516 and no OHT in the winter hemisphere (see Figs. 5 and 7). In other words,
517 when it matters the most, in winter during sea ice expansion, the dynamical
518 ocean does behave like a swamp. Interestingly, even the extremely large heat
519 capacity of the coupled ocean (3000 m deep) is not sufficient to stop the sea
520 ice expansion. This is probably because just before collapse (~ 7500 years,
521 Fig. 12) most of the deep ocean is filled with near freezing waters from the
522 Equator where a small cover of ice is present.

523 *5.3. Implication for the use of EBMs*

524 An interesting result of our simulations is that the total energy transport
525 (THT) in the coupled system is directed down the large-scale temperature
526 gradient at the three obliquities explored here. This occurs despite the oppo-
527 site temperature gradients found at 23.5° and 90° obliquities. At 54° obliquity,
528 both temperature gradients and THT are nearly vanishing, but the tropics
529 are slightly warmer than the poles and the THT is indeed poleward.

530 Our calculations suggest that the use of EBMs in which energy transports
531 are parametrized as down-gradient diffusive processes is justified (Spiegel
532 et al., 2009). This is important as the computationally inexpensive EBMs
533 permit to explore a wide range of parameters which would not otherwise be
534 accessible with a full 3d coupled GCM.

535 There is however an important limitation: the transport efficiency, D ,
 536 relating the THT to the meridional temperature gradient is not a constant,
 537 but is itself a function of the climate. This parameter is often considered
 538 as a tuning parameter and chosen to obtain a good fit to Earth’s present-
 539 day climate (e.g. Williams and Kasting, 1997). Fig. 13 shows scatter plots
 540 of the THT and surface temperature gradients for our Aquaplanets simula-
 541 tions. Estimates (through linear fit) of D at 90° and 23° obliquity are rather
 542 similar, about $0.7\text{--}0.8 \text{ W m}^{-2} \text{ K}^{-1}$.⁶ At $\phi=54^\circ$, D is substantially weaker,
 543 $0.15 \text{ W m}^{-2} \text{ K}^{-1}$. This is not surprising: a significant fraction of the THT is
 544 due to synoptic eddies in the atmosphere spawned by baroclinic instability
 545 which is itself sustained by the large-scale meridional temperature gradient.
 546 Starting with Green (1970) and Stone (1972), there is a large literature link-
 547 ing the eddy diffusivity to the meridional temperature gradient. In Aqua54,
 548 the latter is indeed much weaker than in Aqua23 and Aqua90.

549 This is beyond the scope of the paper to investigate the detailed relation-
 550 ship between the THT and temperature gradients. We emphasize here, that
 551 even in our simple Aquaplanet set-ups, the heat efficiency D varies by more
 552 than a factor 5 across climates. Sensitivities of the results to the choice of D
 553 should be explored when using EBMs.

⁶These values are slightly larger than those typically found in the literature for a
 Earth’s fit, $D \sim 0.4\text{--}0.6 \text{ W m}^{-2} \text{ K}^{-1}$, possibly because of the absence of sea ice in our
 simulations. Estimates of D in colder Aquaplanet configurations with ice-covered poles
 give $D \simeq 0.5 \text{ W m}^{-2} \text{ K}^{-1}$.

554 6. Conclusion

555 We explore the climate of an Earth-like Aquaplanet with high obliquity in
556 a coupled ocean-atmosphere-sea-ice system. For obliquities larger than 54° ,
557 the TOA incoming solar radiation is higher at the poles than at the Equator
558 in annual mean. In addition, its seasonality is very large compared to that
559 found for Earth’s present-day obliquity, $\sim 23.5^\circ$.

560 At 90° obliquity, we find that at all seasons the Equator is the coldest
561 place on the globe and temperatures increase toward the poles. Importantly,
562 the reversed temperature gradients, in thermal wind balance with easterly
563 sheared winds, are large in the summer hemisphere but nearly vanish in the
564 winter hemisphere. This largely reflects the strong gradient of TOA incoming
565 solar radiation in the summer hemisphere but uniform darkness of the winter
566 hemisphere. This is also because the winter atmosphere is uniformly heated
567 by the ocean.

568 As a consequence, the baroclinic zone and storm track activity are con-
569 fined to the midlatitudes of the summer hemisphere. Eddy momentum fluxes
570 associated with the propagation of Rossby wave out of the baroclinic zone
571 maintain surface westerly wind in the midlatitudes of the summer hemi-
572 sphere. Conversely, surface winds nearly vanish in the winter hemisphere.
573 This is in contrast with the 23.5° obliquity Aquaplanet (and present-day
574 Earth) where storm track activity and surface westerly winds are perma-
575 nent in the midlatitudes of the two hemispheres (although weaker in the
576 summer one). The ocean circulation is dominated by its wind-driven com-
577 ponent, and is therefore also confined to the summer hemisphere too. In the
578 winter hemisphere, the ocean is motionless. However, heat stored during the

579 summer in the upper ocean is accessed through convection and released to
580 the atmosphere.

581 Importantly, at large obliquities, both ocean and atmosphere transport
582 energy toward the equator but down the large-scale temperature gradient,
583 as at low obliquities. Similarly to the circulation patterns, these transports
584 are essentially seasonal, large in summer and vanishingly small in winter.
585 In the atmosphere, the transport is achieved by a combination of baroclinic
586 eddies and overturning circulation (which comprises a single cell, extending
587 from 60° in the summer hemisphere to 25°). In the ocean, crucially, the
588 heat transport is carried mainly by the wind-driven circulation. It worth
589 emphasizing that, although the energy transport of the coupled system is
590 always down-gradient in our simulations, the transport efficiency (relating
591 the transport to the temperature gradient as is done in EBMs) is not a
592 constant but varies by a factor 5 across climates.

593 As found in previous studies (e.g. Jenkins, 2000; Williams and Pollard,
594 2003), the surface climate at high obliquities can be relatively mild, provided
595 collapse into a Snowball is avoided. In this case, temperatures at the poles
596 in our Aquaplanet oscillate between 285 and 315 K, clearly in the habitable
597 range. This is primarily explained by the large heat capacity of the surface
598 ocean which stores heat during the summer and releases it to the atmosphere
599 in winter. Although the OHT is substantial and down-gradient, it is of
600 secondary importance in mitigating extreme temperature when compared to
601 the storage effect. This is confirmed by simulations in which the dynamical
602 ocean of our coupled GCM is replaced by a motionless 'swamp' ocean.

603 We found that Snowball collapse is possible whether a dynamical ocean

604 with OHT or a "swamp" ocean is used. Importantly, we could not find
 605 'intermediate' climate state in which a substantial ice cover is present without
 606 a global coverage. This is despite expectations that a dynamical ocean could
 607 stabilize the ice margin in the midlatitudes (Poulsen et al., 2001; Poulsen
 608 and Jacob, 2004; Ferreira et al., 2011). In these studies (all at present-day
 609 obliquity), the large OHT convergence in midlatitudes (due to the wind-
 610 driven circulation) can stop the progression of the sea ice toward the Equator.
 611 In our coupled simulations at high obliquity however, the OHT vanish in the
 612 winter hemisphere at the time of sea ice expansion because surface winds
 613 vanish too. This explains the similarity of the coupled GCM and swamp
 614 ocean simulations. Our results suggest that a state of high obliquity is not
 615 an alternative to the "Snowball Earth" hypothesis to explain evidence of
 616 low-latitude glaciations during the Neoproterozoic.

617 Our simulations employ a configuration without any land. Although it
 618 reproduces (at 23.5° obliquity) the main features of present day climate,
 619 it is plausible that particular continental configurations would have a first
 620 order impact on the climate, for example in cases where large areas of land
 621 are removed from all oceanic influences (e.g. a large polar continent). In
 622 such cases, only the atmospheric heat transport could modulate the extreme
 623 seasonal fluctuations, possibly resulting in temperature excursions beyond
 624 the habitability range. Similarly, we reiterate that we explore here an Earth-
 625 like ocean-atmosphere-sea ice system. We believe that our results are robust
 626 to small changes in parameters around the Earth-like choice used here (say
 627 doubling/halving of eddy diffusion coefficient, rotation rate, etc). Significant
 628 deviation from these values however would require further investigation.

629 Keeping these limitations in mind, it appears that a dynamical ocean
 630 makes little difference whether one is interested in the habitability of exo-
 631 planets or paleoclimate. This suggests that inferences made from simulations
 632 using a "swamp" ocean with no OHT at high obliquity are robust (e.g. Jenk-
 633 ins, 2000, 2003; Donnadieu et al., 2002; Williams and Pollard, 2003). Two
 634 caveats should be noted. First, this conclusion results from the strong season-
 635 ality of the surface winds, itself the consequence of complex atmospheric dy-
 636 namics (conditions for baroclinic instability). This conclusion should not be
 637 extended to other situations without caution. Secondly, although "swamp"
 638 ocean formulation appears to perform similarly to a fully dynamical ocean,
 639 they rely on an ad-hoc choice of a mixed layer depth. In reality, the depth of
 640 the mixed layer is a function of space and time and is determined by ocean
 641 dynamics and air-sea interactions. Unfortunately, the choice of the mixed
 642 layer depth has a direct impact on the solution. In our set-ups, ice-free or
 643 Snowball states can be obtained depending on this choice (with multiple so-
 644 lutions possible for a 50 m deep mixed layer). This is worth keeping in mind
 645 when carrying out such simulations.

646 **7. Appendix: Climate at 54° obliquity**

647 On seasonal scales, atmospheric and oceanic circulations in Aqua54 show
 648 many similarities with those seen at 90° obliquity as both astronomical con-
 649 figurations share an intense contrast in summer/winter solar input.

650 Similarly to Aqua90, surface temperatures in the winter hemisphere re-
 651 main largely above freezing (because of the heat release by the ocean, not
 652 shown) and temperature gradient are very weak throughout the troposphere.

653 In contrast with Aqua90, temperature gradients are also weak in the summer
654 hemisphere, only ~ 10 K (Fig. 14, bottom left, to be compared with Fig. 4,
655 upper left).

656 As a consequence, the synoptic scale activity is weak in both hemispheres
657 as are surface winds in the midlatitudes. As in Aqua90, a Hadley circulation
658 develops with an upper flow from the summer to the winter hemisphere
659 (not shown). It is weaker than in Aqua90 (by a factor 2) as expected from
660 the smaller meridional gradient of incoming solar radiation (see Fig. 1).
661 This cell drives a mirror overturning cell in the ocean (Held, 2001). The
662 mirror ocean-atmosphere overturning circulations explain nearly all of the
663 northward OHT and AHT found in January (Fig. 14, bottom right). Energy
664 transports in both fluids and oceanic MOC are, directly or indirectly, driven
665 by the thermally direct seasonal Hadley circulation which is itself forced by
666 meridional contrasts in solar heating.

667 To the extent that this forcing is linear, the canceling of seasonal contrasts
668 in incoming solar radiation (the annual mean meridional profile is “flat”)
669 leads to a vanishing of the annual mean Hadley circulation, and hence of
670 its AHT and of the oceanic MOC and associated OHT. Indeed, the energy
671 transports in July (not shown) are the opposite of those observed in January
672 and the annual mean values are only a small residual (Fig. 14, top right).

673 Indeed, the annual mean AHT is almost exclusively due to transports by
674 midlatitudes eddies (not shown) but this contribution is four times smaller
675 than in Aqua90 (0.5 PW compared to 2 PW in Fig. 9, top). Nonetheless, the
676 mean energy transports are equatorward, down the (weak) mean temperature
677 gradients.

678 **References**

- 679 Abe, Y., Abe-Ouchi, A., Sleep, N.H., Zahnle, K.J., 2011. Habitable zone
680 limits for dry planets. *Astrobiology* 11, 443–460.
- 681 Adcroft, A., Campin, J., Hill, C., Marshall, J., 2004. Implementation of
682 an atmosphere-ocean general circulation model on the expanded spherical
683 cube. *Mon. Wea. Rev.* 132, 2845–2863.
- 684 Armstrong, J.C., Barnes, R., Domagal-Goldman, S., Breiner, J., Quinn,
685 T.R., Meadows, V.S., 2014. Effects of extreme obliquity variations on
686 the habitability of exoplanets. *Astrobiology* 14, 277–291.
- 687 Bretherton, F.P., 1966. Critical layer instability in baroclinic flows. *Quart.*
688 *J. Roy. Meteor. Soc.* 92, 325–334.
- 689 Campin, J.M., Marshall, J., Ferreira, D., 2008. Sea ice-ocean coupling using
690 a rescaled vertical coordinate z^* . *Ocean Modell.* 24, 1–14.
- 691 Carpenter, R.L., 1964. Study of Venus by CW radar. *The Astronomical*
692 *journal* 69, 2–11.
- 693 Carter, J.A., Winn, J.N., 2010. Empirical constraints on the oblateness of
694 an exoplanet. *The Astrophysical Journal* 709, 1219–1229.
- 695 Correia, A.C.M., Laskar, J., 2011. *Tidal Evolution of Exoplanets*. Exoplan-
696 *ets*, University of Arizona Press.
- 697 Cowan, N.B., Voigt, A., Abbot, D.S., 2012. Thermal phases of earth-like
698 planets: Estimating thermal inertia from eccentricity, obliquity, and diur-
699 nal forcing. *The Astrophysical Journal* 757, 80.

700 Cunha, D., Correia, A.C.M., Laskar, J., 2014. Spin evolution of earth-sized
701 exoplanets, including atmospheric tides and core-mantle friction. *International Journal of Astrobiology* , 1–22.

703 Czaja, A., Marshall, J.C., 2006. The partitioning of poleward heat transport
704 between the atmosphere and ocean. *J. Atmos. Sci.* 63, 1498–1511.

705 Donnadieu, Y., Ramstein, G., Fluteau, F., Besse, J., Meert, J., 2002. Is high
706 obliquity a plausible cause for neoprotozoic glaciations. *Geophys. Res. Lett.* 29, 1–4.

708 Enderton, D., Marshall, J., 2009. Explorations of atmosphere-ocean-ice cli-
709 mates on an aqua-planet and their meridional energy transports. *J. Atmos. Sci.* 66, 1593–1611.

711 Ferreira, D., Marshall, J., Campin, J.M., 2010. Localization of deep water
712 formation: role of atmospheric moisture transport and geometrical constraints on ocean circulation. *J. Climate* 23, 1456–1476.

714 Ferreira, D., Marshall, J., Rose, B., 2011. Climate determinism revisited: multiple equilibria in a complex climate model. *J. Climate* 24, 992–1012.

716 Gaidos, E., Williams, D.M., 2004. Seasonality on terrestrial extrasolar planets: inferring obliquity and surface conditions from infrared light curves. *New Astronomy* 10, 67–77.

719 Gent, P.R., McWilliams, J.C., 1990. Isopycnic mixing in ocean circulation models. *J. Phys. Oceanogr.* 20, 150–155.

721 Green, J.S., 1970. Transfer properties of the large-scale eddies and the general
722 circulation of the atmosphere. *Quart. J. Roy. Meteor. Soc.* 96, 157–185.

723 Held, I., 2000. The general circulation of the atmosphere, in: Woods Hole
724 Oceanographic Institution Geophysical Fluid Dynamics Program, Woods
725 Hole Oceanographic Institution. p. 54.

726 Held, I., 2001. The partitioning of the poleward energy transport between
727 the tropical ocean and atmosphere. *J. Atmos. Sci.* 58, 943–948.

728 Hoffman, P.F., Kaufman, A.J., Halverson, G.P., Schrag, D.P., 1998. A neo-
729 proterozoic snowball earth. *Science* 281.

730 Hoffman, P.F., Schrag, D.P., 2002. The snowball earth hypothesis: testing
731 the limits of global change. *Terra Nova* 14, 129–155.

732 Jenkins, G.S., 2000. Global climate model high-obliquity solutions to the
733 ancient climate puzzles of the faint-young sun paradox and low-altitude
734 proterozoic glaciation. *J. Geophys. Res.* 105.

735 Jenkins, G.S., 2003. Gcm greenhouse and high-obliquity solutions for early
736 proterozoic glaciation and middle proterozoic warmth. *J. Geophys. Res.*
737 108.

738 Kasting, J.F., Kopparapu, R., Ramirez, R.M., Harman, C.E., 2013. Remote
739 life detection criteria, habitable zone boundaries, and the frequency of
740 earthlike planets around m and late-k stars. *Proc. Natl. Acad. Sci.* .

741 Kirschvink, J.L., 1992. Late Proterozoic Low-Latitude Global Glaciation: the

742 Snowball Earth. volume The Proterozoic Biosphere: A Multidisciplinary
743 Study. Cambridge Univ. Press, New York.

744 Klinger, B.A., Marshall, J., Send, U., 1996. Representation of convective
745 plumes by vertical adjustment. *J. Geophys. Res.* C8, 18,175–18,182.

746 Laskar, J., Joutel, F., Robutel, P., 1993. Stabilization of the Earth’s obliquity
747 by the Moon. *Nature* 361, 615–617.

748 Laskar, J., Robutel, P., 1993. The chaotic obliquity of the planets. *Nature*
749 361, 606–612.

750 Marshall, J., Adcroft, A., Campin, J.M., Hill, C., White, A., 2004.
751 Atmosphere-ocean modeling exploiting fluid isomorphisms. *Mon. Wea.*
752 *Rev.* 132, 2882–2894.

753 Marshall, J., Adcroft, A., Hill, C., Perelman, L., Heisey, C., 1997. A finite-
754 volume, incompressible navier stokes model for studies of the ocean on
755 parallel computers. *J. Geophys. Res.* 102, 5753–5766.

756 Marshall, J., Ferreira, D., Campin, J., Enderton, D., 2007. Mean climate
757 and variability of the atmosphere and ocean on an aquaplanet. *J. Atmos.*
758 *Sci.* 64, 4270–4286.

759 Molteni, F., 2003. Atmospheric simulations using a GCM with simplified
760 physical parametrizations. I: model climatology and variability in multi-
761 decadal experiments. *Climate Dyn.* 64, 175–191.

762 North, G.R., Cahalan, R.F., Jr, J.A.C., 1981. Energy balance climate models.
763 *Rev. Geophysics and Space Physics* 19, 91–121.

764 Pauluis, O., 2004. Boundary layer dynamics and cross-equatorial hadley
765 circulation. *J. Atmos. Sci.* 61, 1161–1173.

766 Pierrehumbert, R.T., Abbot, D.S., Voigt, A., Koll, D., 2011. Climate of the
767 neoproterozoic. *Annu. Rev. Earth Planet. Sci.* 39, 417–460.

768 Poulsen, C.J., Jacob, R.L., 2004. Factors that inhibit snowball earth simu-
769 lation. *Paleoceanography* 19, PA4021.

770 Poulsen, C.J., Pierrehumbert, R.T., Jacob, R.L., 2001. Impact of ocean dy-
771 namics on the simulation of the neoproterozoic “snowball earth”. *Geophys.*
772 *Res. Lett.* 28, 1575–1578.

773 Redi, M.H., 1982. Oceanic isopycnal mixing by coordinate rotation. *J. Phys.*
774 *Oceanogr.* 12, 1154–1158.

775 Rose, B.E., Ferreira, D., 2013. Ocean heat transport and water vapor green-
776 house in a warm equable climate: a new look at the low gradient paradox.
777 *J. Climate* 26, 2117–2136.

778 Rose, B.E., Marshall, J., 2009. Ocean Heat Transport, sea ice and multiple
779 climatic states: Insights from Energy Balance Models. *J. Atmos. Sci.* 66,
780 2828–2843.

781 Seager, R., Battisti, D.S., Yin, J., Gordon, N., Naik, N., Clement, A.C.,
782 Cane, M.A., 2002. Is the Gulf Stream responsible for Europe’s mild win-
783 ters? *Quart. J. Roy. Meteor. Soc.* 128, 2563–2586.

784 Seager, S., 2014. The future of spectroscopic life detection on exoplanets.
785 *Proc. Natl. Acad. Sci.* , In press.

786 Shapiro, I.I., 1967. Resonance rotation of venus. *Science* 157, 423–425.

787 Smith, S.K., 2007. The geography of linear baroclinic instability in earth’s
788 oceans. *Journal of Marine research* 65, 655–683.

789 Spiegel, D.S., Menou, K., Scharf, C.A., 2009. Habitable climates: the influ-
790 ence of obliquity. *The Astrophysical journal* 691, 596–610.

791 Stone, P.H., 1972. A simplified radiative-dynamical model for the static
792 stability of rotating atmospheres. *J. Atmos. Sci.* 29, 405–418.

793 Touma, J., Wisdom, J., 1993. The chaotic obliquity of mars. *Science* 259,
794 1294–1297.

795 Trenberth, K.E., Caron, J.M., 2001. Estimates of meridional atmosphere and
796 ocean heat transports. *J. Climate* 14, 3433–3443.

797 Williams, D.M., Kasting, J.F., 1997. Habitable planets with high obliquities.
798 *Icarus* 2, 254–267.

799 Williams, D.M., Pollard, D., 2003. Extraordinary climates of earth-like plan-
800 ets: three-dimensional climate simulations at extreme obliquity. *Interna-*
801 *tional Journal of Astrobiology* 2, 1–19.

802 Winton, M., 2000. A reformulated three-layer sea ice model. *J. Atmos.*
803 *Oceanic Technol.* 17, 525–531.

804 Zsom, A., Seager, S., de Wit, J., Stamenkovic, V., 2013. Toward the mini-
805 mum inner edge distance of the habitable zone. *The Astrophysical Journal*
806 778, 109.

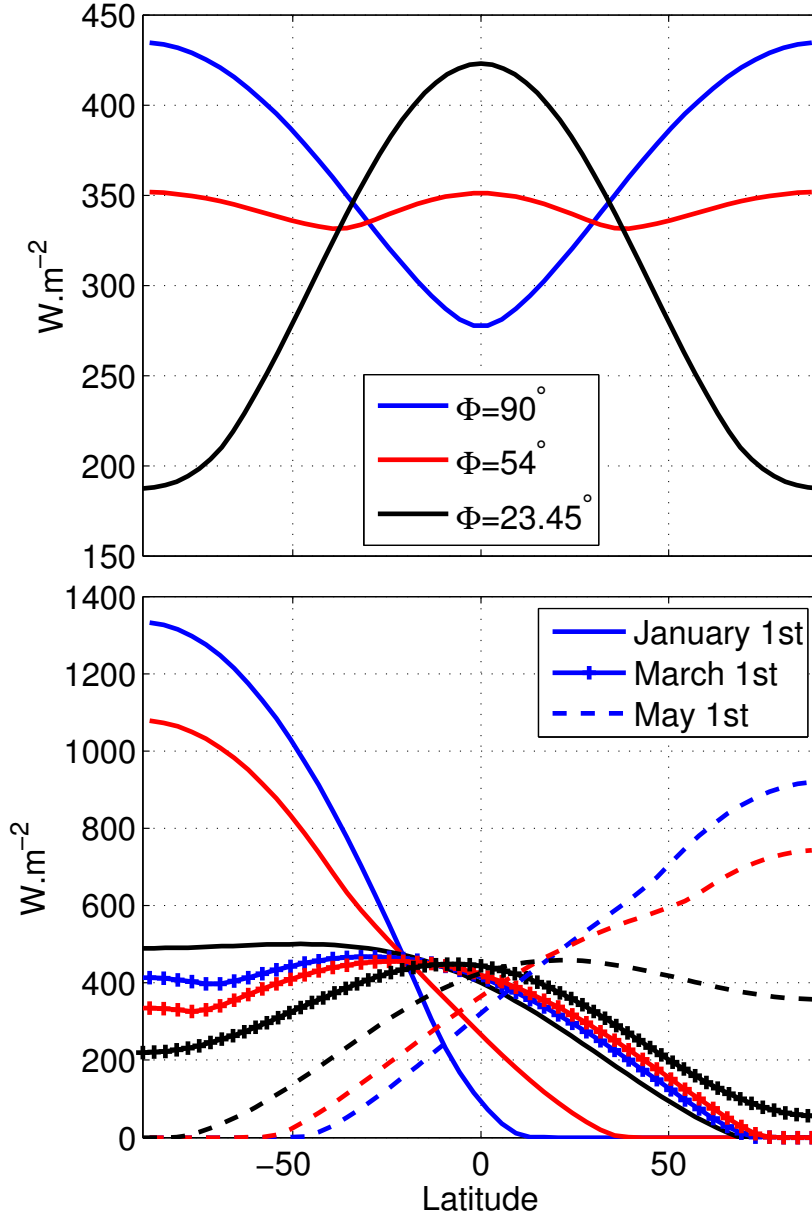


FIG. 1: Top-of-the-atmosphere incoming solar radiation (W m^{-2}) for obliquities of 90° (blue), 54° (red) and 23.45° (black): (top) annual mean and (bottom) daily mean on January 1st (solid), March 1st (dotted), and May 1st (dashed). A zero eccentricity is assumed.

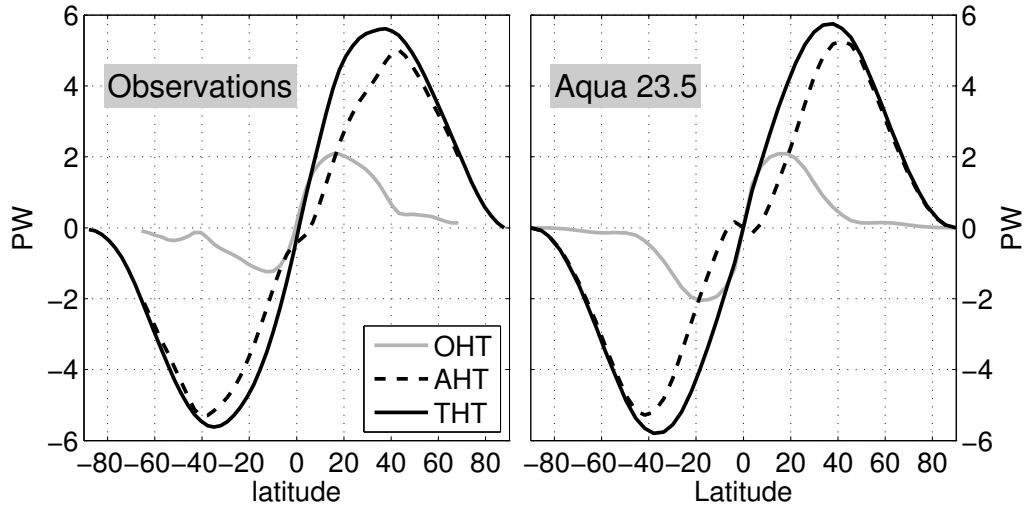


FIG. 2: Ocean, Atmosphere and Total heat transports (in $\text{PW}=10^{15} \text{ W}$) as observed on present-day Earth (left, from Trenberth and Caron (2001)) and in the coupled Aquaplanet GCM with a 23.5° obliquity (right).

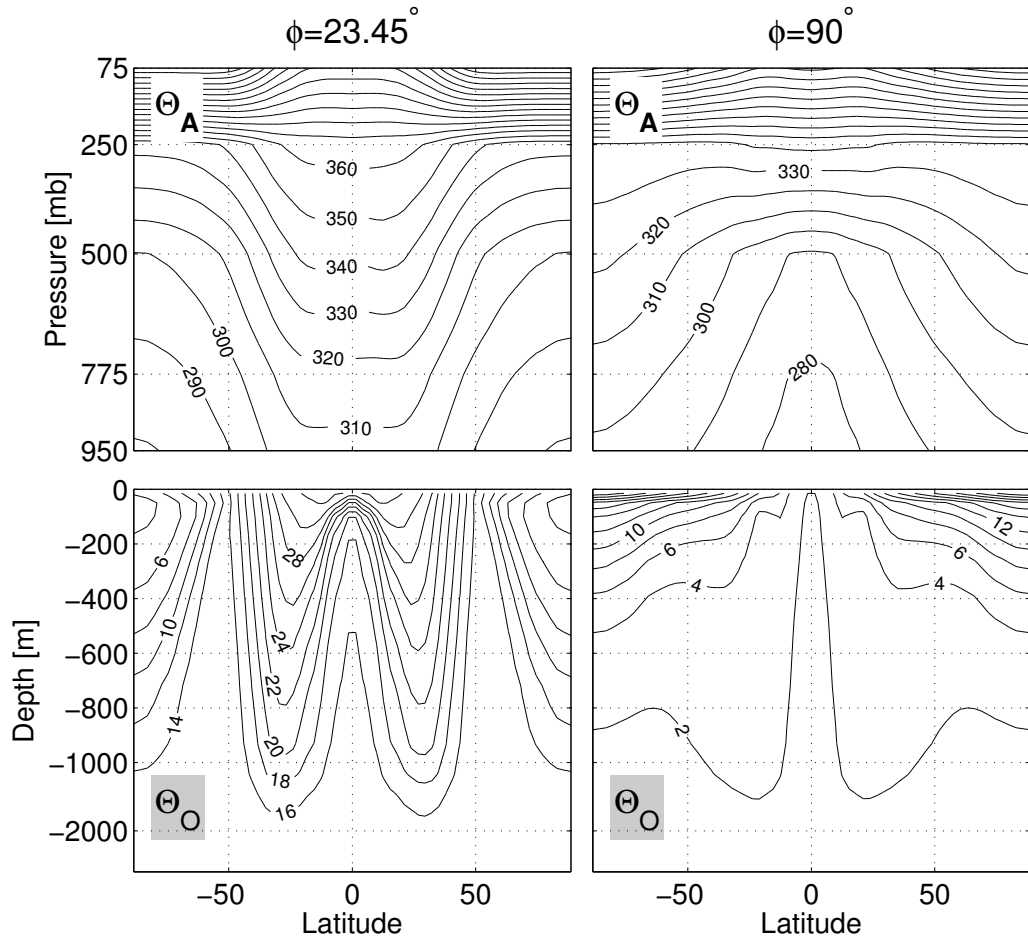


FIG. 3: Zonal and annual averaged atmospheric (top, in K) and oceanic (bottom, in °C) potential temperature in Aqua23 and Aqua90. Note that, in the bottom row, the upper ocean (0-1000 m) is vertically stretched.

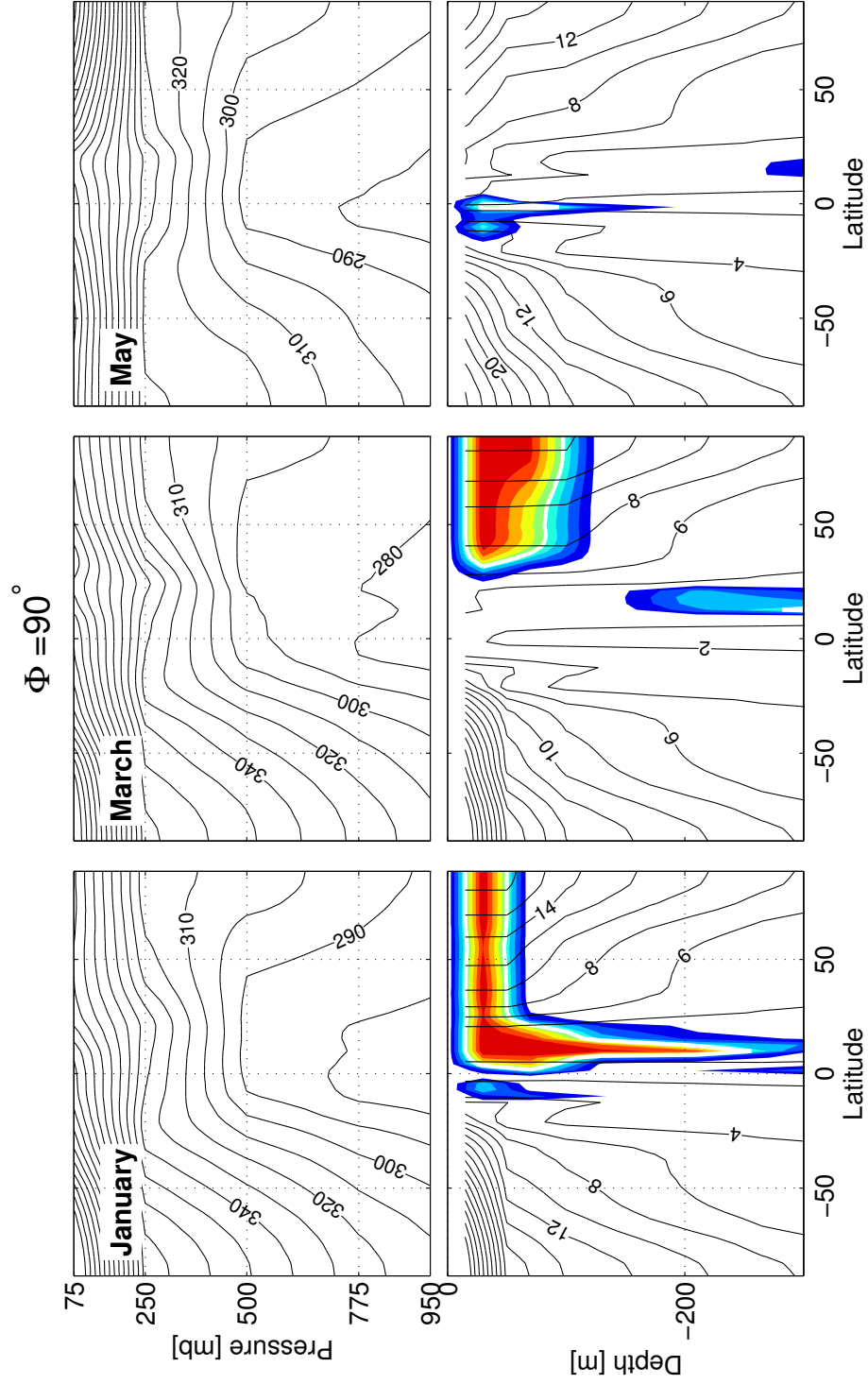


FIG. 4: Zonal mean potential temperature of (top) the atmosphere (in K) and (bottom) of the ocean (in $^{\circ}\text{C}$) in Aqua90: (left) January, (middle) March, and (right) May. Color shading in the ocean denotes the presence of convection. The convective index varies between 100% (red, permanent convection) and 0% (blue, no convection at all). The white contour indicates the 50% value.

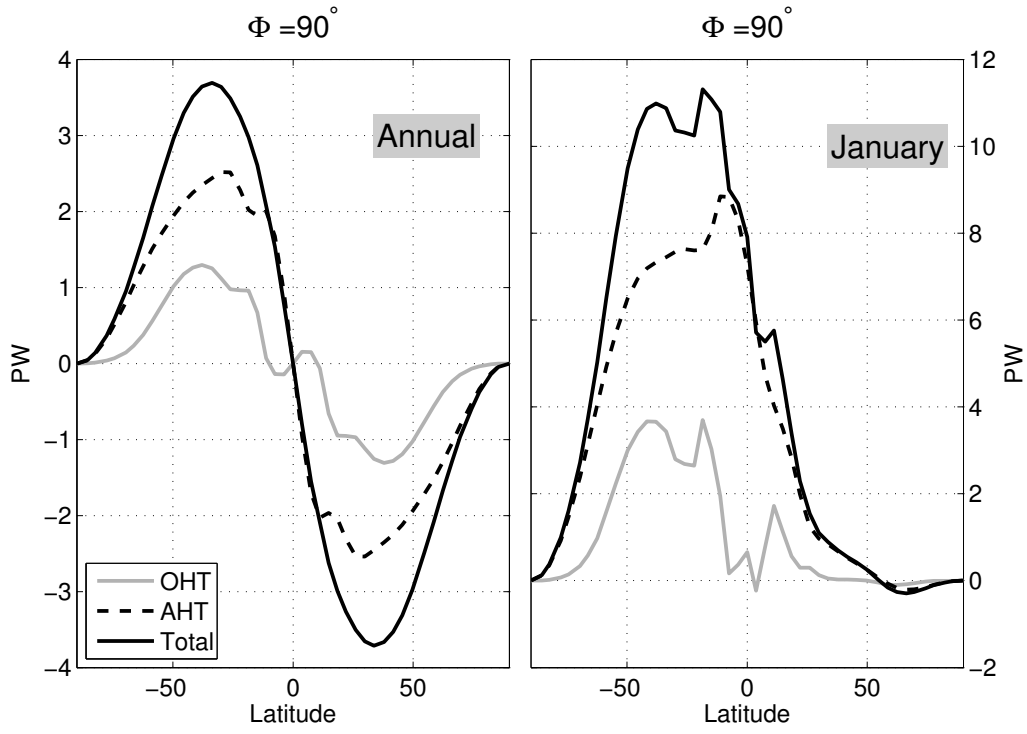


FIG. 5: Annual mean (left) and January mean (right) atmospheric, oceanic and total energy transports in Aqua90. Note the different ordinate scales in the two plots.

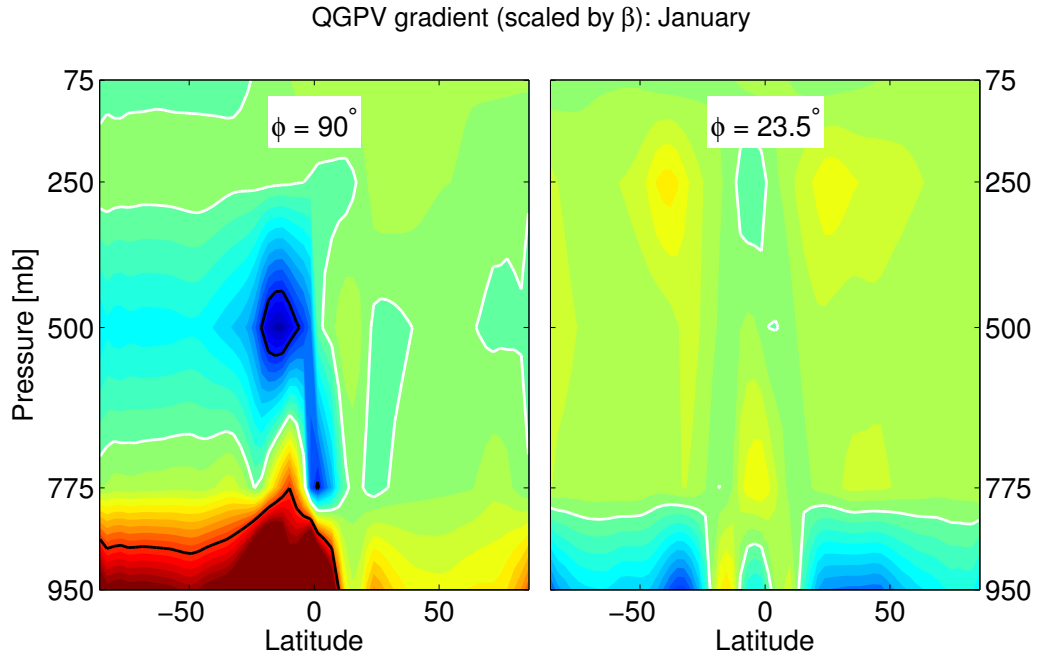


FIG. 6: January zonal mean meridional gradients of QGPV in (left) Aqua90 and (right) Aqua23. The gradients are scaled by the local value of β , the meridional gradient of the Coriolis parameter f . The contour interval is 1. The white and black contours highlight the 0 and ± 10 values, respectively.

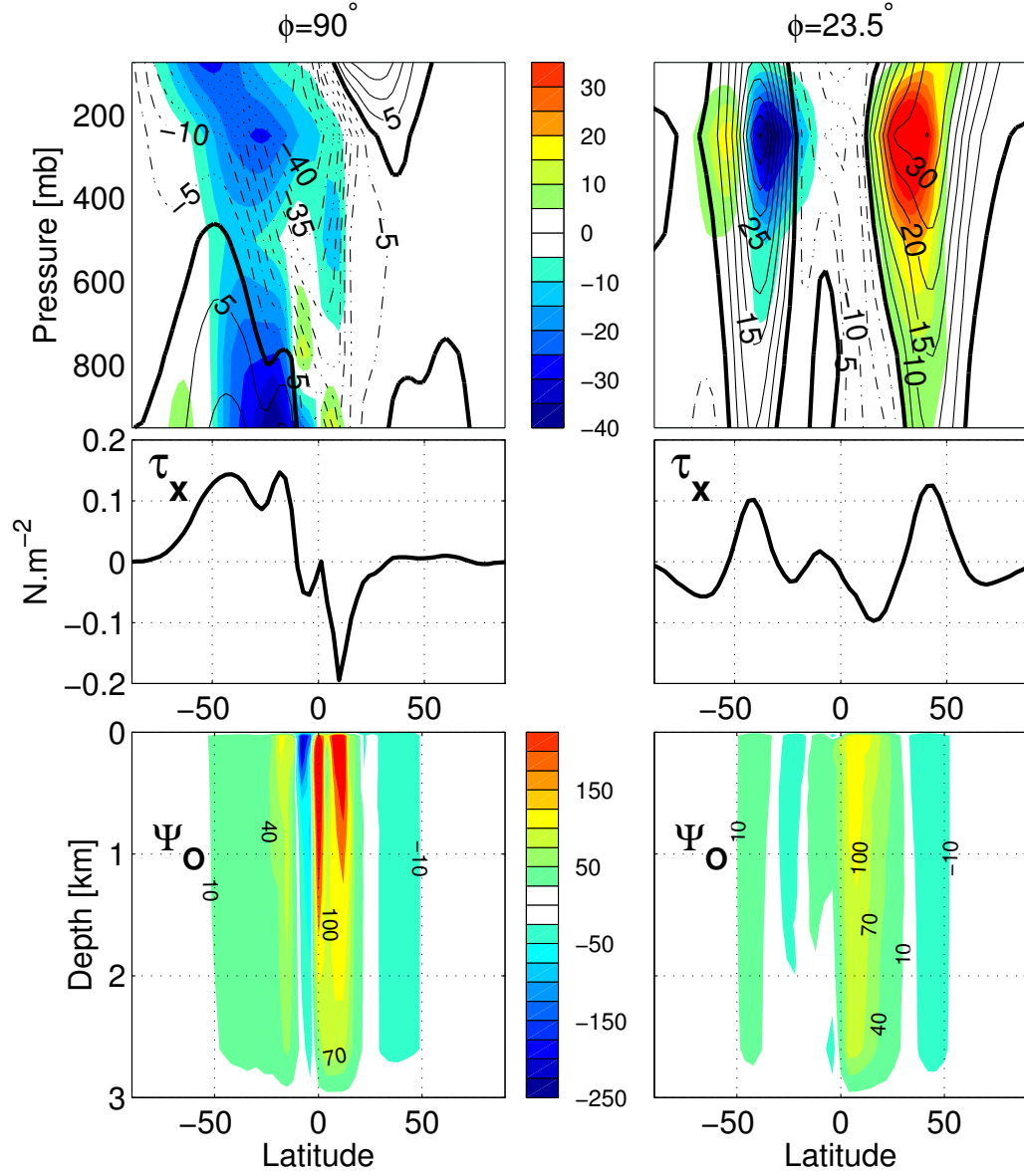


FIG. 7: (top) Zonal mean zonal wind (contours, in m s^{-1}) and Reynolds stresses (shading, in $\text{m}^2 \text{s}^{-2}$), (middle) zonal mean surface wind stress (in N m^{-2}), and (bottom) oceanic Eulerian overturning streamfunction (in Sv) in January in (left) Aqua90 and (right) Aqua23.

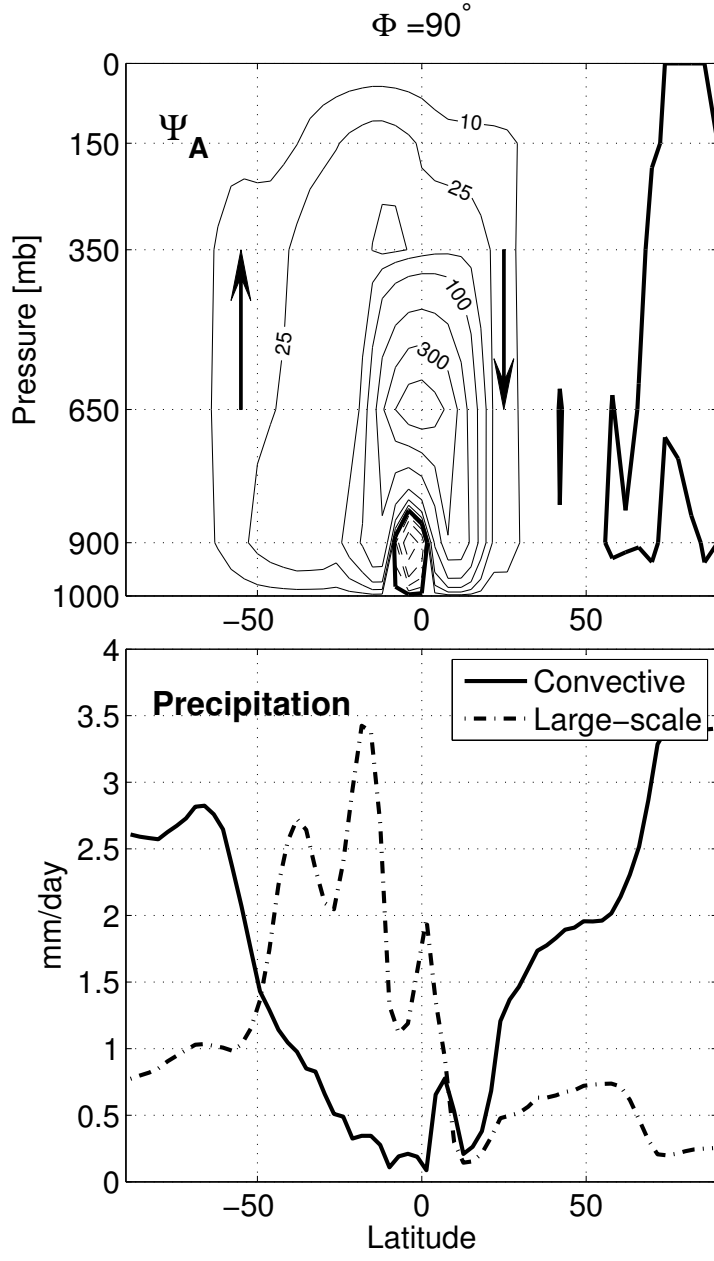


FIG. 8: January mean (top) Atmospheric overturning streamfunction in “atmospheric Sverdrup” ($1 \text{ Sv} = 10^9 \text{ kg s}^{-1}$) and (bottom) convective and large scale precipitation (in mm day^{-1}) in Aqua90.

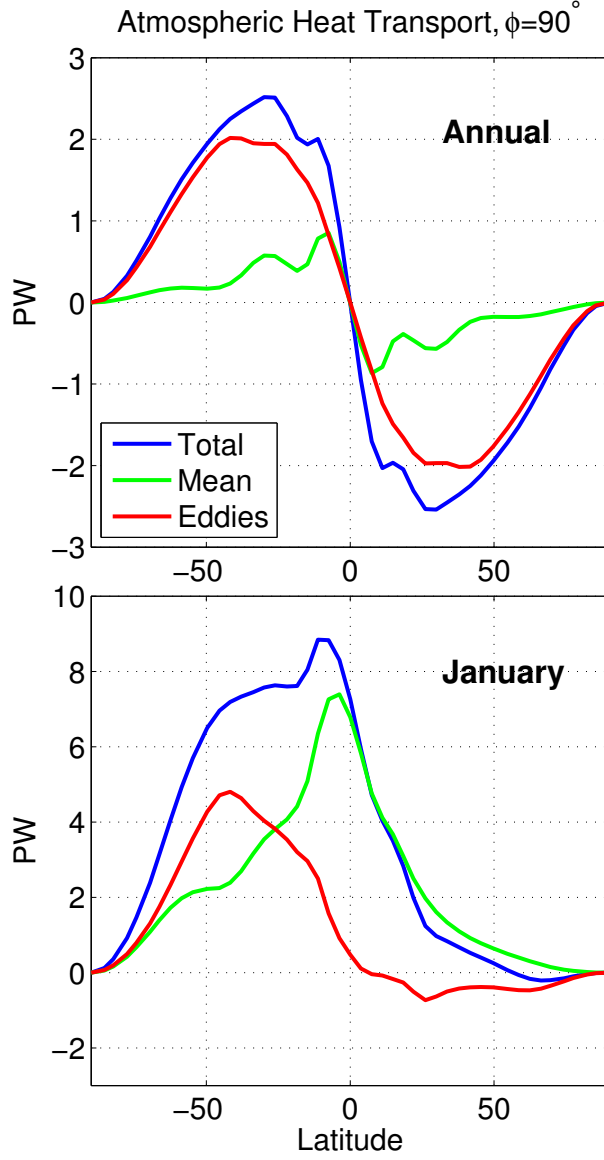


FIG. 9: Decomposition of the atmospheric energy transport AHT into mean and eddy components for the annual mean (top) and January mean (bottom) in Aqua90. Eddies are defined with respect to a zonal and time (monthly) mean. The annual mean eddy contribution is the average of the monthly eddy heat transports.

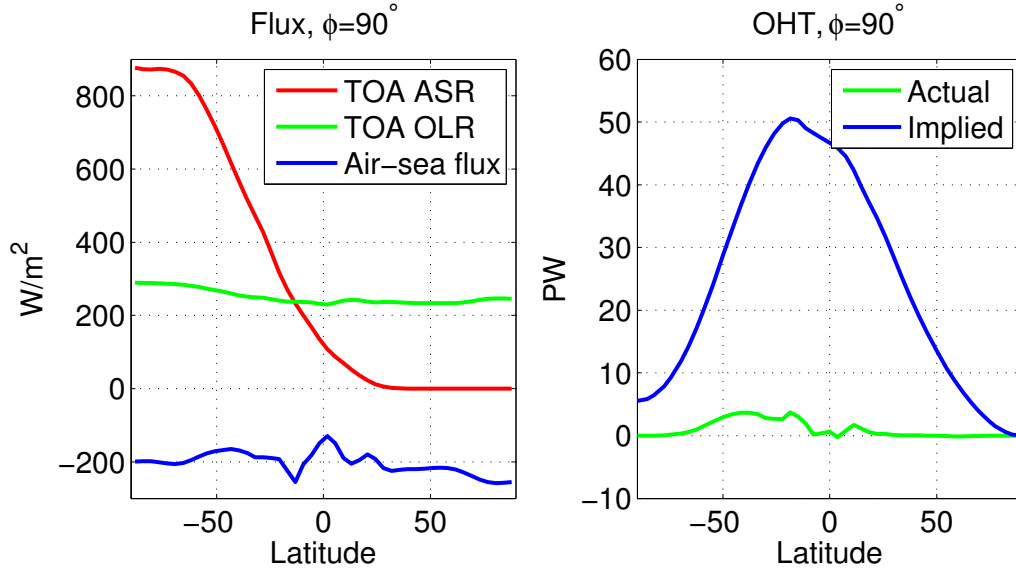


FIG. 10: (left) Top-of-the-atmosphere absorbed shortwave radiation (red), out-going long-wave radiation (green) and surface cooling flux (blue). The latter includes the latent heat, net longwave radiation and sensible heat at the air-sea interface, all three term cool the surface of the ocean. (Right) Actual OHT (green) and OHT implied by the net surface heat flux (blue) in Aqua90 in January. Note that the January OHT is identical to that shown in Fig. 5 (left).

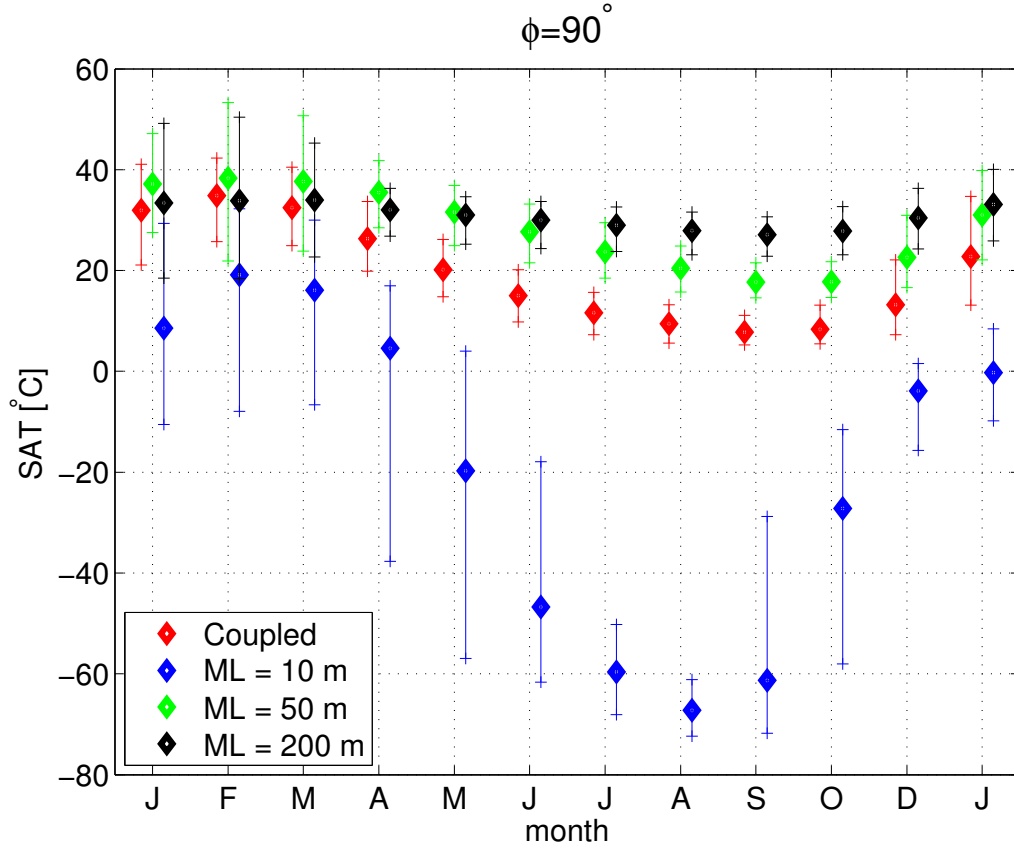


FIG. 11: Mean (diamond) and extreme (+) SAT in the coupled GCM and in the atmosphere-slab ocean runs for each month of the year (compiled over a 20 year period) for the Southern high-latitudes (90°S - 55°S). All simulations uses $\phi=90^\circ$.

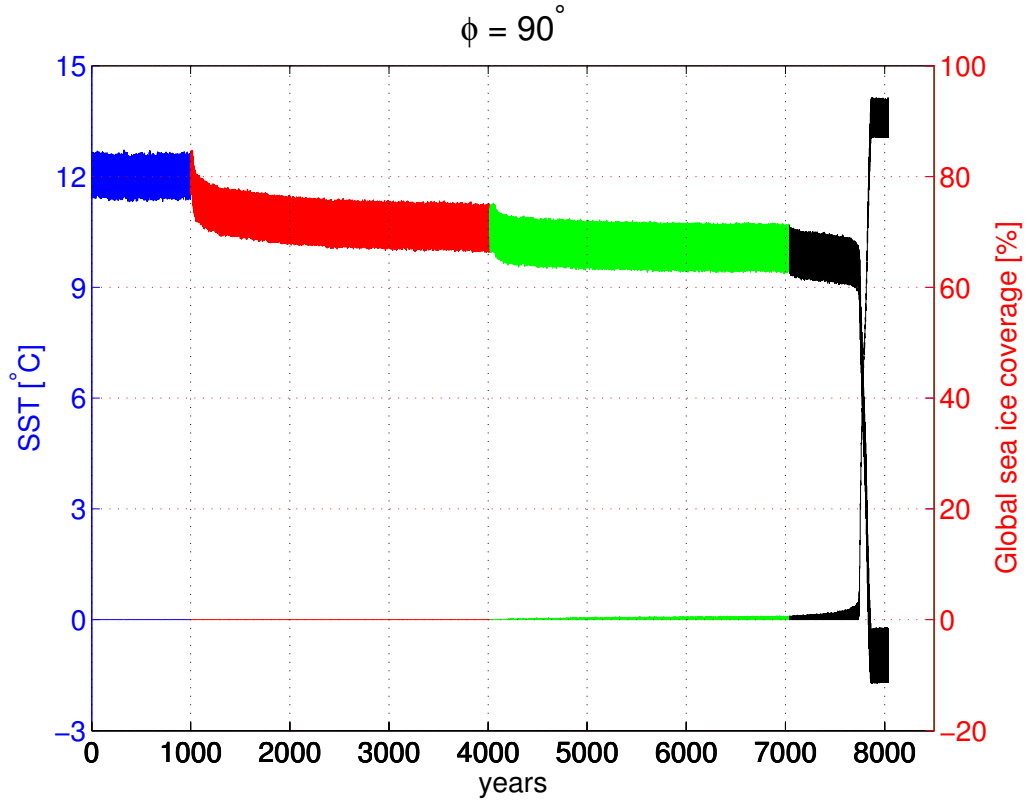


FIG. 12: SST (in $^\circ\text{C}$, upper curve, left axis) and fraction of the globe covered with sea ice (in %, lower curve, right axis) in Aqua90 as the solar constant $S_o/4$ is decreased from 341.5 to 338.0 W m^{-2} .

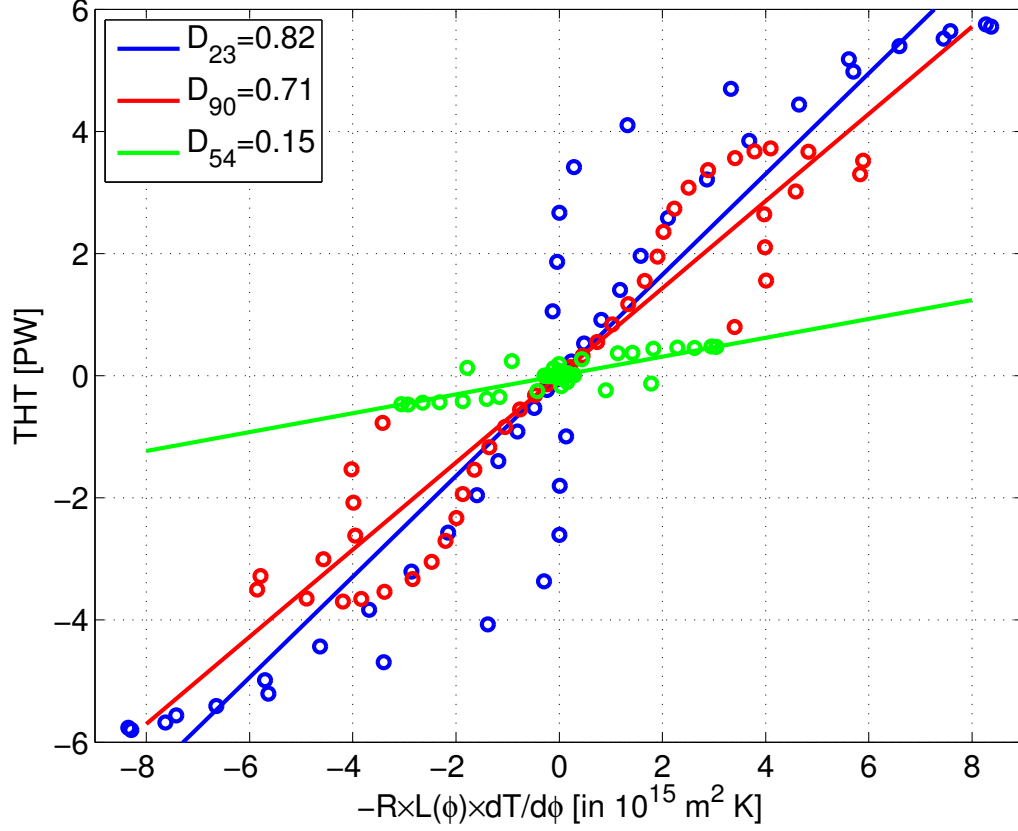


FIG. 13: Scatter plots of the annual-mean THT against the scaled meridional gradient of SAT, $RL(\phi)dT/d\phi$ where $R=6370$ km is the radius of Earth and $L(\phi)$ the length of a latitudinal circle at latitude ϕ for (blue) Aqua23, (red) Aqua90, and (green) Aqua54. Different points correspond to different latitudes. Best linear fits are also shown in solid lines and the estimated slopes D in the upper left box. The coefficient D is expressed in $\text{W m}^{-2} \text{ K}^{-1}$ and is comparable to the heat diffusion parameter used in EBMs (North et al., 1981).

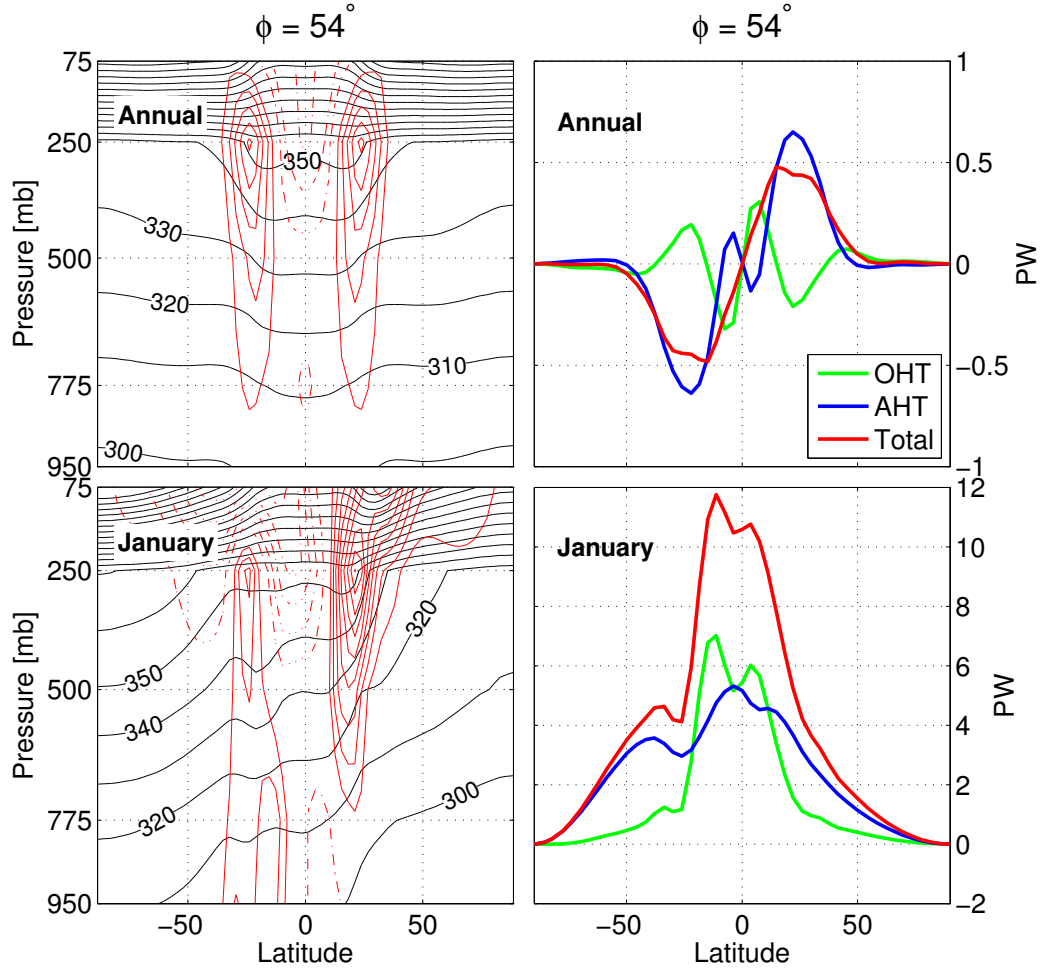


FIG. 14: Aqua54 simulation: (left) potential temperature (K) and zonal mean wind (m s^{-1}) and (right) oceanic, atmospheric and total energy transports. Annual and January averages are shown at the top and bottom, respectively.